hand, islands in experimentally determined Poincaré cuts become visible on the order of 10^1 to 10^2 circulation times and initial placement is less critical. In the experiments the streaklines are stretched into sheets or ribbons and are repeatedly folded in the chaotic regions, revealing typical striated patterns in the Poincaré section. A streakline on a torus is stretched into a ribbon along the surface of the torus; thus, the entire island is revealed in only a few circulations. This flow is successful because the azimuthal circulation time (driven by impeller) and the rate of rotation of the tori are of comparable orders of magnitude (ratio of about 3.5 in our experiments). The robustness of these analog (experimental) simulations lies in their ability to produce connected structures, as opposed to the "peppered-like" appearance of computational results involving the tracking of single particles. Errors in the visualization result from the disturbance in the flow produced by the presence of injection needles, from vibrations, and from geometrical imperfections in the apparatus. Yet, even with these experimental factors, tori generated with the needles in place remain nearly unchanged with time even after 12 hours of operation.

Theoretical analysis with existing tools seems possible only in limiting cases. The unperturbed flow is integrable because of rotational symmetry. For small α and moderate *Re* the experimental results can be treated in terms of perturbation theory of action-angle-angle volume-preserving flows developed by Mézic and Wiggins (*31*). Topological ideas based on flow skeleton arguments, which encapsulate the underlying mathematical structure in terms of fixed points and manifolds, may prove useful as well (*16*).

References and Notes

1. G. B. Tatterson, R. S. Brodkey, R. V. Calabrese, *Chem. Eng. Prog.* **87(6)**, 45 (1991).
2. L. H. Kellogg, *Adv. Geophys.* **34**, 1 (1993).
3. M. Manga, *Geophys. Res. Lett.* **23**, 403 (1996).
4. H. J. Yang and Z. Y. Liu, *ibid.* **21**, 545 (1994).
5. M. G. Brown and K. B. Smith, *Phys. Fluids A* **3**, 1186 (1991).
6. R. B. Pierce and T. D. A. Fairle, *J. Geophys. Res. Atmos.* **98**(D10), 18589 (1993).
7. R. T. Pierrehumbert and H. Yang, *J. Atmos. Sci.* **50**, 2462 (1993).
8. J. M. Ottino *et al.*, *Science* **257**, 754 (1992).
9. J. M. Ottino, *Annu. Rev. Fluid Mech.* **22**, 207 (1990).
10. ———, C. W. Leong, H. Rising, P. D. Swanson, *Nature* **333**, 419 (1988).
11. H. A. Kusch and J. M. Ottino, *J. Fluid Mech.* **236**, 319 (1992).
12. D. J. Lamberto, F. J. Muzzio, P. D. Swanson, *Chem. Eng. Sci.* **51**, 733 (1996).
13. H. Aref, *J. Fluid Mech.* **143**, 1 (1984).
14. S. Wiggins, in *Chaotic Transport in Dynamical Systems* (Springer-Verlag, New York, 1992).
15. M. Hénon, *C. R. Acad. Sci. Paris A* **262**, 312 (1966).
16. R. S. MacKay, *J. Nonlinear Sci.* **4**, 329 (1994).
17. P. Ashwin and G. P. King, *J. Fluid Mech.* **338**, 341 (1997).
18. G. Haller and I. Mézic, *Nonlinearity* **11**, 319 (1998).
19. K. Bajer and H. K. Moffat, *J. Fluid Mech.* **212**, 337 (1990).
20. H. A. Stone, A. Nadim, S. H. Strogatz, *ibid.* **232**, 629 (1991).
21. This flow can be achieved, for example, near the stagnation point of impinging circular jets.
22. J. M. Ottino, *The Kinematics of Mixing: Stretching, Chaos, and Transport* (Cambridge Univ. Press, New York, 1989), pp. 146–148.
23. S. Nagata, *Mixing: Principles and Applications* (Wiley, New York, 1975); G. B. Tatterson, *Fluid Mixing and Gas Dispersion in Agitated Tanks* (McGraw-Hill, New York, 1991).
24. R. C. DiPrima and H. L. Swinney, *Topics in Applied Physics*, H. L. Swinney and J. P. Gollub, Eds. (Springer-Verlag, New York, 1985), vol. 45, pp. 139–180.
25. G. K. Batchelor, *An Introduction to Fluid Dynamics* (Cambridge Univ. Press, New York, 1967), pp. 290–294.
26. P. D. Swanson and J. M. Ottino, *J. Fluid Mech.* **213**, 227 (1990).
27. The supporting sleeve is connected by a series of gears to a motor, allowing rotation in either direction. The impeller is constructed of a 10.16-cm-diameter 0.46-cm-thick acrylic disk mounted on a 1/2-inch (1.27-cm) aluminum shaft that is mounted with a 2.5-cm-tall needle bearing to prevent radial movement. Both motors are controlled manually with Bodine speed controls. An outer rectangular containment vessel is used to minimize optical effects due to curvature.
28. A Liconix 4240NB helium-cadmium constant-wave laser is used with 442-nm blue optics installed. The power rating at this wavelength is a nominal 40 mW and is verified at 36 mW with an Ophir Optronics laser power meter. The sheet is created by using a cylindrical lens mounted on the laser head and aligned such that the sheet falls on the center line of the impeller shaft.
29. C. E. Willert and M. Gharib, *Exp. Fluids* **10**, 181 (1991), see also special issue on Particle Image Velocimetry, J. Kompenhaus and C. Tropea, Eds., *Meas. Sci. Technol.* **8** (December 1997).
30. Each needle has a small radius bend ~3 cm from the end to allow it to project horizontally into the flow. Pressurizing the supply chambers feeding the needles controls the injection rate. To prevent dye "tails" upon repositioning or removal of the needles, the supply pressure is removed and a slight vacuum is applied.
31. I. Mézic and S. Wiggins, *J. Nonlinear Sci.* **4**, 157 (1994).

32. We thank R. Lueptow for assistance with the PIV measurements and I. Mézic for providing comments on a draft of this paper. Supported by the U.S. Department of Energy, Division of Basic Energy Sciences.

25 March 1998; accepted 7 May 1998

Ultraslow Electron Spin Dynamics in GaAs Quantum Wells Probed by Optically Pumped NMR

N. N. Kuzma, P. Khandelwal, S. E. Barrett,* L. N. Pfeiffer, K. W. West

Optically pumped nuclear magnetic resonance (OPNMR) measurements were performed in two different electron-doped multiple quantum well samples near the fractional quantum Hall effect ground state $\nu = \frac{1}{3}$. Below 0.5 kelvin, the spectra provide evidence that spin-reversed charged excitations of the $\nu = \frac{1}{3}$ ground state are localized over the NMR time scale of about 40 microseconds. Furthermore, by varying NMR pulse parameters, the electron spin temperature (as measured by the Knight shift) could be driven above the lattice temperature, which shows that the value of the electron spin–lattice relaxation time τ_{1s} is between 100 microseconds and 500 milliseconds at $\nu = \frac{1}{3}$.

A two-dimensional electron system (2DES), cooled to extremely low temperatures in a strong magnetic field, exhibits many exotic phenomena, such as the fractional quantum Hall effect (FQHE) (*1*). Transport and optical studies of the 2DES have shown that the low-energy physics in these extreme conditions is driven by the electron-electron Coulomb interaction (*2*), but the challenge of precisely describing the low-lying many-body states that exist in a real 2DES remains formidable for both theory and experiment (*3–5*). Such 2DESs have been probed by OPNMR (*6–8*) in the FQHE regime (*9*), which allows the direct radio-frequency (rf) detection of NMR signals from nuclei in electron-doped GaAs quantum wells. The ^{71}Ga OPNMR spectra reveal the local, time-averaged value of the electron spin magnetization, $\langle S_z(\mathbf{R})\rangle$, thus leading to insights about the many-electron states relevant for the FQHE.

We report evidence of ultraslow electron spin dynamics near the most studied FQHE ground state, $\nu = \frac{1}{3}$, with characteristic time scales exceeding ~40 μs below 0.5 K. Although the samples are characterized by "simple" NMR parameters (that is, isotropic

N. N. Kuzma, P. Khandelwal, S. E. Barrett, Department of Physics, Yale University, New Haven, CT 06511, USA. L. N. Pfeiffer and K. W. West, Lucent Technologies, Bell Laboratories, Murray Hill, NJ 07974, USA.

*To whom correspondence should be addressed.

hyperfine coupling in an oriented single crystal), the OPNMR spectra are complex because they can simultaneously exhibit inhomogeneous broadening due to the quantum confinement of electrons within a well and motional narrowing due to delocalization of electrons along the well (*10*). At low temperatures ($T \approx 0.5$ K), a change in the NMR linewidth is observed whenever spin-reversed electrons are present. We attribute this behavior to the localization of spin-reversed electrons over the NMR time scale. In addition, using the Knight shift as a thermometer, we measured the increase of the electron spin temperature above the lattice temperature when rf pulses were used to drive the system out of equilibrium. These nonequilibrium measurements imply that the electron spin–lattice relaxation time is 100 μs $< \tau_{1s} <$ 500 ms for $T < 0.5$ K at $\nu = \frac{1}{3}$, which appears to exceed all electronic time scales previously measured in semiconductors by at least a factor of 1000.

Both of the multiple quantum well samples in this study were grown by molecular beam epitaxy on semi-insulating GaAs(001) substrates. Sample 40W contained 40 300 Å wide GaAs wells that were separated by 3600 Å wide $Al_{0.1}Ga_{0.9}As$ barriers. Sample 10W contained 10 260 Å wide wells that were separated by 3120 Å wide barriers. Silicon delta-doping spikes located at the center of each barrier provided the electrons that were confined in each GaAs well at low temperatures, producing a 2DES with very high mobility ($\mu > 1.4 \times 10^6$ cm^2 V^{-1} s^{-1}) (*11*). The 2D electron densities in each well were $n_{40W} = 6.69 \times 10^{10}$ cm^{-2} and $n_{10W} = 7.75 \times 10^{10}$ cm^{-2} (*9*).

The low-temperature (0.29 K $< T <$ 1.5 K), high-field (B_{tot} = 12 T) OPNMR measurements were performed with an Oxford Instruments sorption-pumped ^{3}He cryostat that was mounted in a Teslatron^{H} superconducting magnet. The samples, about 4 mm by 6 mm by 0.5 mm, were in direct contact with helium and were mounted on the platform of a rotator assembly in the NMR probe. By tilting this platform, we could vary the angle θ ($-60° < \theta < 60°$, $\pm 0.1°$) between the sample's growth axis $\mathbf{z'}$ (perpendicular to the plane of the wells) and the applied field $\mathbf{B}_{tot}$ (fixed along $\mathbf{z}$), thereby changing the filling factor $\nu = (nhc)/(eB_{\perp})$ in situ (here $B_{\perp} \equiv B_{tot} \cos \theta$), where h is Planck's constant, c is the speed of light, and e is the electron charge. For optical pumping, light from a Coherent 890 Ti:sapphire laser was delivered into the cryostat through an optical fiber (*12*), which was terminated by a collimating lens and a polarizing assembly 22 cm above the sample. The light spot on the sample (5 mm diameter, 812 nm wavelength, left-circularly polarized, $\leq$10 mW cm^{-2}) was gated by a spectrometer-controlled room-temperature shutter.

For the OPNMR measurements, we used the timing sequence SAT-τ_L-τ_D-DET (*6–9*); SAT denotes an rf pulse train that destroys (saturates) the ^{71}Ga nuclear polarization throughout the sample, τ_L is light time, τ_D is dark time, and DET denotes the detection period. During τ_L (30 to 90 s), optical pumping of interband transitions generated electrons and holes in the GaAs wells with nonequilibrium spin polarizations, which then polarized the nuclei in the wells through the hyperfine interaction. The shutter was then closed to allow the electrons to equilibrate with the ^{3}He bath during τ_D (typically 40 s). The enhanced nuclear polarization persisted until DET, whereupon a single rf tipping pulse was applied to produce a free induction decay signal, which we then acquired with a homebuilt NMR spectrometer that was based on a Tecmag Aries system. A calibrated RuO_2 thermometer, in good thermal contact with the sample, recorded the temperature during signal acquisition.

A ^{71}Ga OPNMR emission spectrum at $\nu = \frac{1}{3}$ (Fig. 1A, solid line) exhibits a "w" peak that arises from nuclei in the GaAs quantum well and a "b" peak that is due to nuclei in the $Al_{0.1}Ga_{0.9}As$ barriers (*7–9*). The Fermi contact hyperfine coupling between the spins of the 2DES and nuclei in the well shifts the w peak below the b peak by K_S, which we define to be the Knight shift (*10, 13*). The asymmetry of the well line shape has two origins: (i) the quantum confinement within the well causes the electron density to vary across its width w as $\rho(z') \approx \cos^2(\pi z'/w)$ for $|z'| \leq w/2$ (*14, 15*) and (ii) the optical pumping preferentially polarizes nuclei in the center of the well. Taking these two effects into account, the intrinsic line shape (Fig. 1A, hatched region) may be written as the sum of $I_w^{int}(K_{Sint}, f) = [f/(K_{Sint} - f)]^{1/2}$ and $a_b\delta(0)$ for the unbroadened barrier signal. Using a 3.5-kHz full width at half maximum (FWHM) Gaussian $g(f)$ for the nuclear dipolar broadening (*10*), we arrive at a two-parameter fit (Figs. 1 and 2, dashed lines):

$$I(f) = I_b + I_w = a_b g(f) + \int_0^{K_{Sint}} df' g(f - f') I_w^{int}(K_{Sint}, f') \quad (1)$$

The first parameter, a_b, is the amplitude of the barrier signal, which grows during τ_L as the optically pumped nuclear magnetization diffuses out of the quantum well. The second parameter extracted from the fit is the hyperfine shift for nuclei in the center of the well, $K_{Sint}(\nu, T) = \mathcal{P}(\nu, T)(n/w)(4.5 \pm 0.2) \times 10^{-16}$ kHz cm^3 (*9*). Thus, fits to OPNMR spectra at various ν and T provide a direct measure of the electron spin polarization $\mathcal{P}(\nu, T) \equiv \langle S_z(\nu, T)\rangle / \max\langle S_z \rangle$ in the quantum well.

This approach has been used to map out $\mathcal{P}(\nu, T)$ in the vicinity of important integer and fractional quantum Hall ground states of $\nu = 1$ and $\nu = \frac{1}{3}$. The $\mathcal{P}(T)$ measurements at fixed ν revealed the neutral spin-flip excitations of the fully polarized ground states. Measurements of $\mathcal{P}(\nu)$ provided the first evidence (*7, 8*) of the existence of skyrmions (*16, 17*), which are charged spin-texture excitations of the $\nu = 1$ ground state (*5*). Recently, $\mathcal{P}(\nu)$ was found to drop on either side of the $\nu = \frac{1}{3}$ ground state, which shows that the charged excitations of this FQHE ground state are partially spin reversed, even in a 12-T field (*9*).

In all of these earlier measurements, the OPNMR spectra were well described by the dashed-line fits generated by our model. The central assumption of this model is that the electron spins are delocalized along the well, such that $\langle S_z(\nu, T)\rangle$ appears spatially homogeneous when averaged over the NMR time scale (~40 μs) (*18*). In this limit, the delocalization of the low-density 2DES (there are ~10^6 nuclei per electron in the well) produces a motional narrowing of I_W^{int}.

However, low-temperature measurements at $\nu = 0.267$ showed a crossover to more complicated line shapes (Fig. 1B). Although the spectra were in reasonable agreement with our model above 1 K, the width of the w peak increased dramatically as the temperature was lowered to $T = 0.45$ K and then

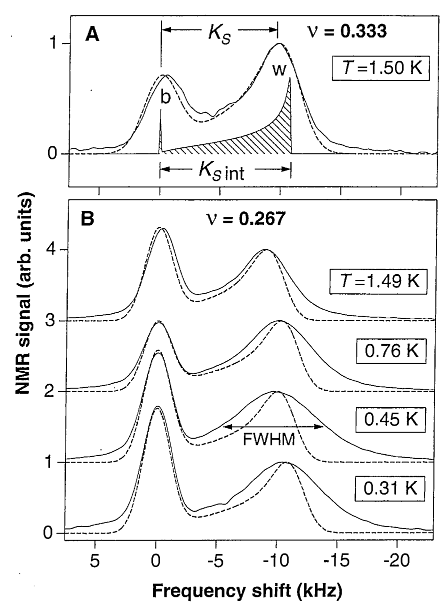

Fig. 1. (**A**) The ^{71}Ga OPNMR emission spectrum (solid line) of sample 10W at $\nu = \frac{1}{3}$, taken at θ = 36.8° in B_{tot} = 12 T. The frequency shift is relative to f_o = 155.93 MHz. The dashed line fit is obtained by broadening the intrinsic line shape (hatched region). Empirically, $K_{Sint} = K_S + 1.1[1 - \exp(-K_S/2.0)]$ (in kilohertz). (**B**) Temperature dependence of the spectra at ν = 0.267 (θ = 0°). The FWHM of the well resonance w peak is shown. Arb. units, arbitrary units.

decreased upon further lowering to $T = 0.31$ K. This nonmonotonic temperature dependence is reminiscent of the behavior seen in NMR studies of systems in which spectra are sensitive to dynamical processes (*19*), variously referred to as motional narrowing, dynamical averaging, or chemical exchange (*10, 20, 21*). In our experiment, the nuclei were rigidly fixed in the lattice of a single crystal, so the variation in the line shape shown in Fig. 1B was a signature of electron spin localization, which turned off the motional narrowing of the well resonance as the temperature was lowered.

The extra broadening of the well resonance disappeared as the sample was tilted from $\theta_{10W} = 0°$ ($\nu = 0.267$) to 36.8° ($\nu = \frac{1}{3}$) (Fig. 2), despite a 10% increase in the dipolar broadening [the ^{75}As nearest neighbors of the ^{71}Ga nuclei are at the "magic angle" (*21*) when $\theta_{10W} = 0°$]. Furthermore, there was a correspondence between the decrease in the linewidth and the increase in K_S as $\nu \rightarrow \frac{1}{3}$ (Fig. 3). This anticorrelation strongly suggests that the behavior shown in Figs. 1 to 3 is due to electron spin dynamics.

For a quantitative understanding of these phenomena, we must consider the specific assumptions that lead to $I_W^{\text{int}}(K_{\text{Sint}}, f)$. Nuclei within the well couple to the spins of the 2DES through the isotropic Fermi contact interaction (*6–10*); thus, a nucleus at site $\mathbf{R}'$ experiences a hyperfine magnetic field $\mathbf{B}^e(\mathbf{R}') = (-16\pi\mu_B/3)\Sigma_j \mathbf{S}_j \delta(\mathbf{r}_j - \mathbf{R}')$, where μ_B is the Bohr magneton, $\mathbf{S}_j$ is the spin of electron j, the summation is over all of the conduction electrons within the well, and the delta function picks out those electrons that overlap with the nucleus at $\mathbf{R}'$. The average projection of $\mathbf{B}^e$ along the applied field $\mathbf{B}_{\text{tot}}$ may be written quite generally as $\langle B_z^e(\mathbf{R}', \nu, T)\rangle = [(-8\pi\mu_B)/3]\,(n/w)\,[|^{71}u(0)|^2|\chi(Z')|^2|\phi(X', Y')|^2]\,\mathcal{P}(\mathbf{R}', \nu, T)$. Here, the probability density of finding electrons at a ^{71}Ga site has been factored into a term with the periodicity of the lattice $|^{71}u(0)|^2$ and terms that vary slowly within a unit cell $|\chi(Z')|^2|\phi(X', Y')|^2$ (*13*). $\mathcal{P}(\mathbf{R}', \nu, T)$ is the local spin polarization ($-1 < \mathcal{P} < 1$) of the electrons at $\mathbf{R}'$. If we assume that electrons are delocalized along the well, then the time-averaged values of $|\phi|^2$ and $\mathcal{P}$ are spatially homogeneous. In this limit, the local hyperfine frequency shift (taken to have the sign of $\mathcal{P}$) is a function of z' only, $[f(z') = -^{71}\gamma\langle B_z^e(z', \nu, T)\rangle/2\pi \approx \cos^2(\pi z'/w)\, K_{\text{Sint}}]$, so the general expression for the well line shape is $I_W^{\text{int}}(f') = \Sigma_{N\text{-wells}} \int d^3r' \langle ^{71}I_z(z')\rangle\, \rho_{\text{nuclear}}\delta[f' - f(z')]$. We further assume that wells are identical and that the optical pumping gives rise to a nuclear polarization that varies across each well as $\langle\langle ^{71}I_z(z')\rangle\rangle \propto f(z')$, which leads to the form $I_W^{\text{int}}(f') = [f'/(K_{\text{Sint}} - f')]^{1/2}$ (shown in Fig. 1A).

The observed broadening of the well line shape beyond the motionally narrowed limit implies that the time-averaged value of $|\phi|^2\mathcal{P}$ becomes spatially inhomogeneous. Although the $|\phi(X', Y')|^2$ term could become inhomogeneous if a pinned Wigner crystal were to form, the corresponding increase in the linewidth (by orders of magnitude) and the concomitant drop in the peak intensity are not observed. Furthermore, variations in charge density along the well (for example, arising from fluctuations in the dopant layer) do not appear to explain either the magnitude of the effect (*22*) or the nonmonotonic temperature dependence. In contrast, the Knight shift data show that the total spin polarization drops monotonically below $\nu = \frac{1}{3}$, allowing the local spin polarization $\mathcal{P}(\mathbf{R}')$ to be spatially inhomogeneous. Thus, we conclude that localization of spin-reversed regions is responsible for the behavior shown in Figs. 1 to 3.

The time scale of the spin localization may be inferred by simulating the observed line shapes. In our model, for every point (x', y') along the plane of the well, the local polarization is either up ($\mathcal{P} = 1$) or down ($\mathcal{P} = -0.15$). After every jump time τ_J, the local polarization instantaneously assumes either the up or down value with probability p_+ or $(1 - p_+)$, respectively. At all times, the ratio of up to down sites is $p_+/(1 - p_+)$. The simulated OPNMR spectra depend on the value of τ_J, as is shown in Fig. 4 for the case $p_+ = 0.85$. The simulation is in reasonable agreement with the corresponding data from sample 10W. When τ_J is very fast, all nuclei see the same time-averaged local polarization, which is equal to the total polarization ($\mathcal{P}_{\text{total}} = 0.828$ at $\nu = 0.275$ for our assumptions). At the other extreme ($\tau_J \rightarrow \infty$), the motion is frozen out, and the single resonance is split into up and down lines, with areas proportional to p_+ and $(1 - p_+)$, respectively. Even within this simple model, the inhomogeneous breadth of the frozen line shape (owing to the quantum confinement) leads to a nontrivial evolution of the spectrum in the intermediate motion regime (for example, a given value of τ_J might be simultaneously "fast" for nuclei at the edge of the well and "slow" for nuclei in the center of the well). In the intermediate motion regime, the FWHM of the w peak goes through a maximum when $\tau_J = 40$ μs. Although varying the parameters p_+ and K_{Sint} (over the range relevant for samples 10W and 40W) affects the extreme value of the FWHM, the characteristic τ_J remains ~40 μs.

On the basis of this simple model, the peaks in the FWHM at $T_{\text{loc}} \approx 0.5$ K (Fig. 3) reflect the localization temperature of reversed spins, such that they fail to cover the sample uniformly over ~40 μs. The self-similar curves in Fig. 3 suggest that T_{loc} is not a strong func-

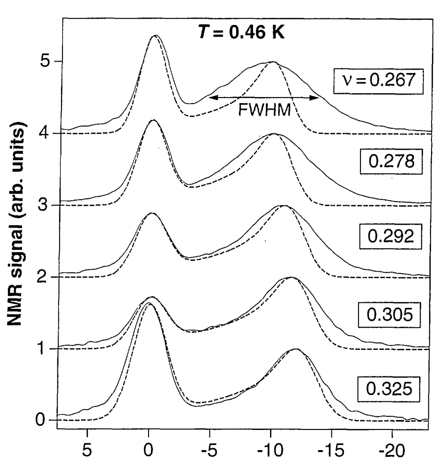

Fig. 2. The ^{71}Ga OPNMR spectra (solid lines) of sample 10W at $T = 0.46$ K, for $0.267 \leq \nu < \frac{1}{3}$ ($0° \leq \theta < 36.8°$).

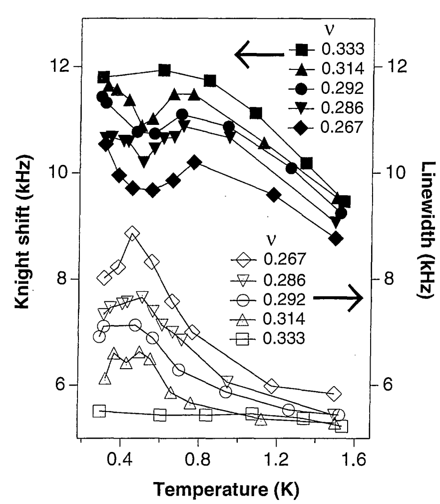

Fig. 3. The temperature dependence of the Knight shift (solid symbols) and the linewidth (open symbols) for several filling factors $0.267 \leq \nu \leq \frac{1}{3}$ in sample 10W. Lines are to guide the eye.

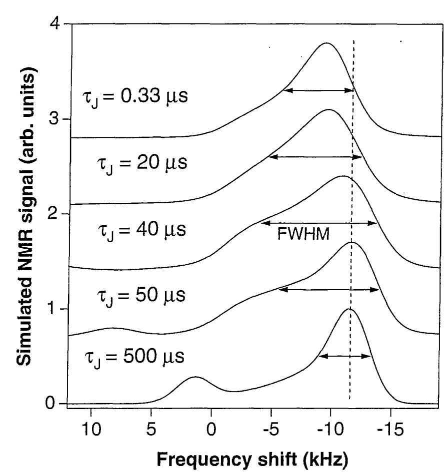

Fig. 4. OPNMR spectra simulated with the model described in the text. K_{Sint} is set to 12 kHz for $\mathcal{P} = 1$. The barrier is suppressed ($a_b = 0$) for clarity.

tion of the filling factor (or the density of reversed spins) for $\nu < \frac{1}{3}$. Below 0.5 K, the measured $K_S(\nu < \frac{1}{3})$ increases toward $K_S(\nu = \frac{1}{3})$, as seen in the model. However, even down to $T = 0.3$ K, the spectra do not appear to match the frozen limit of our simulation. As ν is varied below $\frac{1}{3}$, the trends in the K_S and FWHM data (Fig. 3) continue smoothly through $\nu = \frac{2}{7}$ without interruption. High-field magnetotransport measurements of samples taken from the same wafer as 10W show much more structure, with well-developed minima in ρ_{xx} at $\nu = \frac{1}{3}, \frac{2}{5}, \frac{2}{7}$, and $\frac{1}{5}$ at $T = 0.3$ K (*11, 23*).

Additional measurements of the linewidth for $\nu > \frac{1}{3}$ in sample 10W were consistent with the above picture. Measurements in sample 40W for $\nu \leq \frac{1}{3}$ were also in qualitative agreement, with one important quantitative difference: T_{loc} appeared to be shifted lower, so that only the high-temperature side of the peak in the FWHM was observed down to $T \approx 0.3$ K. There was a similar sample variation in the saturation temperature of $\mathcal{P}(\frac{1}{3})$, with $T^{sat}_{10W} \approx 0.77$ K and $T^{sat}_{40W} \approx 0.46$ K. The observed spectra contain more information than our simple simulation has revealed. A more sophisticated model might include (i) a detailed structure for the reversed spin regions present below $\nu = \frac{1}{3}$, (ii) the 2D dynamics of these reversed spins, and (iii) the effects of thermally excited spin flips, because T_{sat} is not that much greater than T_{loc}.

All of the results described thus far were acquired by applying a weak rf tipping pulse long after optical pumping to probe the equilibrium properties of the 2DES. Nonequilibrium properties of the electron spin system can be studied by varying these parameters at low temperatures, with a number of notable results at $\nu = \frac{1}{3}$.

The rf tipping pulse for the NMR experiment is produced by a coil wrapped around the sample (Fig. 5C, inset), which generates a linearly polarized (perpendicular to $\mathbf{z}'$) magnetic field of amplitude $2 \times H_1$ at $f_o = 155.93$ MHz. The equilibrium value of $K_S(T)$ is independent of the tipping pulse parameters for weak H_1 (that is, $H_1 \approx 5$ G, $\tau_{pulse} = 20$ μs). However, if stronger pulses are used for $T < 0.5$ K, the measured K_S value drops sharply below the equilibrium value, even though the lattice temperature is unaffected by the pulses. The equilibrium measurements (*9*) of $K_S(T)$ (Fig. 5, A and B) can be used to convert the measured K_S into an effective electron spin temperature T_{spin}; T_{spin} rises linearly above the lattice temperature T as the duration of the tipping pulse τ_{pulse} increases, for $H_1 \approx 7$ G (Fig. 5, C and D). The increase of T_{spin} drops off sharply with increasing lattice temperature and is not observable for $T > 0.5$ K. Furthermore, the apparent heating depends strongly on the alternating field strength and scales as H_1^{η} $(2 < \eta < 5)$, which rules out nuclear spins as the heat source, because their tipping angle scales as $H_1 \times \tau_{pulse}$. Another possible mechanism, ohmic heating by eddy currents, appears to be inconsistent with the strong T and H_1 dependence of the effect. Rather, these data provide evidence for a direct coupling between the rf pulse and the spins in the 2DES. The mechanism for this interaction in a clean system is not known, because the applied rf photon energy is well below the electron spin resonance at ~74 GHz. Impurities in the bulk or edge states may be involved in this process.

The nonequilibrium spectra remain motionally narrowed and appear to be indistinguishable from the corresponding equilibrium spectra measured at a higher lattice temperature. Thus, the electron spin system achieves internal equilibrium before our measurement, justifying our use of T_{spin} (*10*). However, our measurement also shows that T_{spin} remains greater than T long after the rf pulse is turned off, which implies that the electron spin–lattice relaxation time τ_{1s} is greater than 100 μs for $T < 0.5$ K at $\nu = \frac{1}{3}$.

The evolution of the spectra as the dark time τ_D is increased provides an upper bound on τ_{1s} (Fig. 6). The measured spectra are essentially independent of τ_D after the first 0.5 s, which is consistent with the equilibration time of the laser-heated sample with the helium bath at 0.45 K. Combining these results, we find 100 μs $< \tau_{1s} <$ 500 ms for $T < 0.5$ K at $\nu = \frac{1}{3}$. Although this value of τ_{1s} is at least a factor of 1000 longer than recent measurements of the transverse relaxation time τ_2^* in bulk GaAs (*24*), it is consistent with a previous theoretical prediction (*25*) that had assumed conditions similar to those in our experiment.

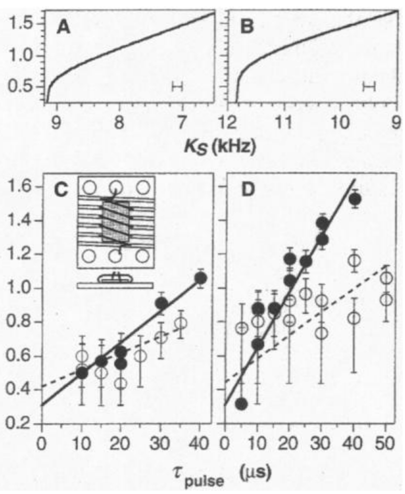

Fig. 5. $T(K_S)$ calibration curves based on the equilibrium $K_S(T)$ data for (**A**) sample 40W and (**B**) sample 10W. Error bars for K_S are shown. The dependence of the effective spin temperature on the rf pulse length ($H_1 \approx 7$ G) for (**C**) sample 40W and (**D**) sample 10W. The intercept of the straight line fit was constrained to be the lattice temperature: $T = 0.31$ K (solid circles 10W and 40W), $T = 0.42$ K (open circles 40W), and $T = 0.44$ K (open circles 10W). The inset (C) shows the top (along $\mathbf{z}'$) and the front (along the rotation axis) views of the grooved sapphire platform holding a sample in a five-turn rf coil.

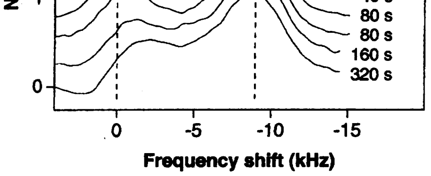

Fig. 6. Spectra, which were acquired with sample 40W at $T_{bath} = 0.45$ K, that show the evolution of the line shape as a function of dark time τ_D.

References and Notes

1. D. C. Tsui, H. L. Stormer, A. C. Gossard, *Phys. Rev. Lett.* **48**, 1559 (1982).
2. R. B. Laughlin, *ibid.* **50**, 1395 (1983).
3. T. Chakraborty and P. Pietiläinen, *The Quantum Hall Effects: Fractional and Integral* (Springer-Verlag, Berlin, ed. 2, 1995).
4. R. E. Prange and S. M. Girvin, Eds., *The Quantum Hall Effect* (Springer-Verlag, New York, ed. 2, 1990).
5. S. Das Sarma and A. Pinczuk, Eds., *Perspectives in Quantum Hall Effects* (Wiley, New York, 1997).
6. S. E. Barrett, R. Tycko, L. N. Pfeiffer, K. W. West, *Phys. Rev. Lett.* **72**, 1368 (1994).
7. S. E. Barrett *et al.*, *ibid.* **74**, 5112 (1995).
8. R. Tycko, S. E. Barrett, G. Dabbagh, L. N. Pfeiffer, K. W. West, *Science* **268**, 1460 (1995).
9. P. Khandelwal, N. N. Kuzma, S. E. Barrett, L. N. Pfeiffer, K. W. West, *Phys. Rev. Lett.* **81**, 673 (1998); also available at xxx.lanl.gov/abs/cond-mat/9801199.
10. C. P. Slichter, *Principles of Magnetic Resonance* (Springer-Verlag, New York, ed. 3, 1990).
11. L. N. Pfeiffer *et al.*, *Appl. Phys. Lett.* **61**, 1211 (1992).
12. D. Heiman, in *The Spectroscopy of Semiconductors*, D. G. Seiler and C. L. Littler, Eds. (Academic Press, San Diego, CA, 1992), chap. 1.
13. J. Winter, *Magnetic Resonance in Metals* (Oxford Univ. Press, London, 1971).
14. C. Weisbuch and B. Vinter, *Quantum Semiconductor Structures* (Academic Press, San Diego, CA, 1991).
15. G. Fishman, *Phys. Rev. B Condens. Matter* **27**, 7611 (1983).
16. S. L. Sondhi, A. Karlhede, S. A. Kivelson, E. H. Rezayi, *ibid.* **47**, 16419 (1993).
17. H. A. Fertig, L. Brey, R. Côté, A. H. MacDonald, *ibid.* **50**, 11018 (1994).
18. For nuclei in the center of the well, $\mathcal{P}$ can fluctuate between −1 and 1, resulting in local frequency variations of $\pm K_{Sint}$. Thus, the NMR time scale that separates fast and slow fluctuations is $\sim(2K_{Sint})^{-1} \approx 40$ μs.
19. A. Abragam, *Principles of Nuclear Magnetism* (Oxford Univ. Press, New York, 1961).
20. J. I. Kaplan and G. Fraenkel, *NMR of Chemically Exchanging Systems* (Academic Press, New York, 1980).

21. M. Mehring, *Principles of High Resolution NMR in Solids* (Springer-Verlag, Berlin, ed. 2, 1983).
22. In simulations, we found that an unreasonably large FWHM of 35% was required for a Gaussian distribution of electron densities along the well to explain the maximum NMR linewidth observed at $\nu = 0.267$.
23. R. L. Willett, private communication.
24. J. Kikkawa and D. Awschalom, *Phys. Rev. Lett.* **80**, 4313 (1998).
25. D. M. Frenkel, *Phys. Rev. B Condens. Matter* **43**, 14228 (1991).
26. We thank S. M. Girvin, D. A. Huse, A. H. MacDonald, N. Read, S. Sachdev, and S. L. Sondhi for helpful discussions and K. E. Gibble, R. L. Willett, and K. W. Zilm for assistance with experiments. Supported by NSF CAREER grant DMR-9501925.

24 March 1998; accepted 24 June 1998

Near Extinction of a Large, Widely Distributed Fish

Jill M. Casey and Ransom A. Myers*

Are extinctions of marine vertebrates as rare and unlikely as current data indicate? Long-term research surveys on the continental shelf between the Grand Banks of Newfoundland and southern New England reveal that one of the largest skates in the northwest Atlantic, the barndoor skate (*Raja laevis*), is close to extinction. Forty-five years ago, research surveys on St. Pierre Bank (off southern Newfoundland) recorded barndoor skates in 10% of their tows; in the last 20 years, none has been caught, and this pattern of decline is similar throughout the range of the species.

Elasmobranchs, such as sharks and rays, tend to be very susceptible to the effects of fishing because they generally grow slowly, mature late in life, and produce few offspring (*1*). Species of the family Rajidae, although the most fecund of the elasmobranchs (*2*), are known to experience varying degrees of resilience to exploitation (*3*) because of the large range in life history characteristics within this family. Although shark fisheries usually cause a sharp decline in species abundance (*4*), dogfish and skates on Georges Bank have increased in biomass after the depletion of groundfish stocks (*5*). It has been suggested that the energy released into the ecosystem by these depleted stocks has provided resources for elasmobranch populations to increase. The recent introduction of a directed fishery for dogfish and skate on Georges Bank, however, has resulted in a marked decline of these species (*6*).

The barndoor skate, *Raja laevis*, is one of the largest skates in the northwest Atlantic (*7*), and it ranges from Cape Hatteras to the Grand Banks of Newfoundland (Fig. 1). Once common (*8*), this distinctive species, with a maximum body width of just over 1 m, now appears to be near extinction. Although the extinction of marine species is thought to be rare (*9*), the closely related "common" skate in the northeast Atlantic, *Raja batis*, was shown to be locally extinct in the Irish Sea (*10*). If current population trends continue, however, the barndoor skate could become the first well-documented example of extinction in a marine fish species.

Biomass (in kilograms per square kilometer) of the barndoor skate (Fig. 2) was determined from research vessel surveys (*11*) that have been conducted in the spring on the southern Grand Bank and St. Pierre Bank since 1951, in the summer on the Scotian Shelf since 1970, and in the autumn from Georges Bank to southern New England since 1963. The population trend is similar for all regions, with biomass decreasing into the early 1970s, after which barndoor skates were caught only on Browns Bank and nearby Georges Bank (*12*).

The longest time series available are for the southern Grand Bank, at the species' northern limit on the continental shelf, and St. Pierre Bank, where barndoor skates were once commonly found. Compared with other skate species on St. Pierre Bank, the barndoor skate had been one of the most numerous skates, second in abundance only to the thorny skate (*Raja radiata*) (*13*). If we consider the mean biomass of the barndoor skate in each decade and the corresponding mean weight of individuals on St. Pierre Bank, the average number of barndoor skates in the 1950s would have been on the order of 0.6 million. That number would decrease to about 0.2 million individuals in the 1960s and to less than an estimated 500 individuals in the 1970s. The other smaller skate species, namely thorny skate and smooth skate (*Raja senta*), were actually increasing in biomass over this time period.

The mean weight of individual skates on St. Pierre Bank is a good indicator of their vulnerability to commercial trawls. Species large enough to be caught in trawls have been decreasing in size over the time period, whereas the size of the smallest species, the smooth skate, has remained fairly constant. The regulated mesh size on commercial fishing gear has ranged from 7 to 14 cm over the survey period, although a smaller mesh size has been used illegally (*14*). The barndoor skate is vulnerable to commercial trawls from hatching at a length of about 20 cm (*7*).

Direct biological information on skates in the northwest Atlantic is scarce. Sufficient comparative information, however, is available to estimate the mortality required to drive this species to extinction. The closest relative of the barndoor skate in the North Atlantic, the common skate (*7*), matures at about 11 years (*10*). We should expect a similar age at maturity on Georges Bank, which has a similar temperature regime (*15*). Maximum egg production, which can be estimated from the inverse relation with the weight of the young at hatching (*16*), is about 47 eggs per year.

Considering the age at maturity and the annual fecundity of the barndoor skate, the

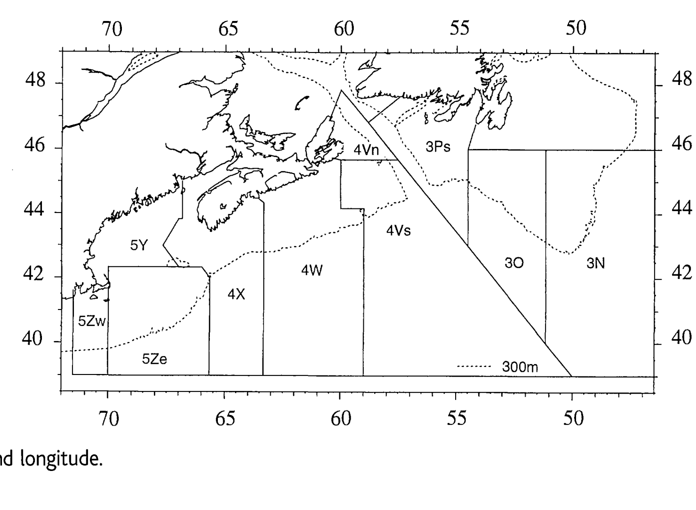

Fig. 1. Map of the Northwest Atlantic Fisheries Organization. Subdivisions in which populations were assessed in this analysis are shown. The 300-m isobath (dotted line) is given for reference. 3N and 3O, southern Grand Bank; 3Ps, St. Pierre Bank; 4Vn, Sydney Bight; 4Vs, Banquereau Bank; 4W, Sable Island Bank; 4X, Browns Bank; 5Y, Gulf of Maine; 5Ze, Georges Bank; 5Zw, southern New England. The numbers on the axes are degrees of latitude and longitude.

J. M. Casey, Department of Biology, Memorial University of Newfoundland, St. John's, Newfoundland, Canada A1C 5S7. R. A. Myers, Department of Biology, Dalhousie University, Halifax, Nova Scotia, Canada B3H 4J1.

*To whom correspondence should be addressed. E-mail: ransom.myers@dal.ca